

Topological Floquet Engineering of Twisted Bilayer Graphene

Gabriel E. Topp,¹ Gregor Jotzu,¹ James W. McIver,¹ Lede Xian,¹ Angel Rubio,^{1,2} and Michael A. Sentef^{1,*}

¹*Max Planck Institute for the Structure and Dynamics of Matter,
Luruper Chaussee 149, 22761 Hamburg, Germany*

²*Center for Computational Quantum Physics (CCQ),
The Flatiron Institute, 162 Fifth Avenue, New York NY 10010*

(Dated: April 19, 2022)

We investigate the topological properties of Floquet-engineered twisted bilayer graphene above the magic angle driven by circularly polarized laser pulses. Employing a full Moiré-unit-cell tight-binding Hamiltonian based on first-principles electronic structure we show that the band topology in the bilayer, at twisting angles above 1.05° , essentially corresponds to the one of single-layer graphene. However, the ability to open topologically trivial gaps in this system by a bias voltage between the layers enables the full topological phase diagram to be explored, which is not possible in single-layer graphene. Circularly polarized light induces a transition to a topologically nontrivial Floquet band structure with the Berry curvature of a Chern insulator. Importantly, the twisting allows for tuning electronic energy scales, which implies that the electronic bandwidth can be tailored to match realistic driving frequencies in the ultraviolet or mid-infrared photon-energy regimes. This implies that Moiré superlattices are an ideal playground for combining twistronics, Floquet engineering, and strongly interacting regimes out of thermal equilibrium.

I. INTRODUCTION

Light-matter coupled systems are emerging as an important research frontier bridging condensed matter physics [1], quantum optics [2–6], as well as cold atoms in optical lattices [7–9]. In ultrafast materials science, intriguing phenomena have been explored, including but not limited to ultrafast switching between different phases of matter [10–12], light control of important couplings in solids [13–15], and light-induced superconductivity [16, 17]. In cavities, spectacular effects have been observed or predicted, such as dramatically enhanced conductivity in polymers [18], cavity-modified materials properties [19–22], novel spectroscopies using the quantum nature of light [5], or light-controlled chemical reaction pathways [23]. Finally, in optical lattices, periodically driven quantum systems are investigated within the realm of Floquet engineering, in which the driving is used as a tool to generate effective Hamiltonians with tunable interactions [24–28], which has also been demonstrated in purely photonic systems [29].

In solids, key progress has been made for instance in observing Floquet-Bloch states in time-resolved photoemission spectroscopy [30] or with the recently demonstrated light-induced anomalous Hall effect in graphene under circularly polarized laser driving [31–33]. However, the concept of Floquet engineering of a material’s topological properties [34–43] has been limited to very few material systems so far. The reason for this is that the time and energy scales often cause problems in avoiding resonant excitations and accompanying heating effects that are usually detrimental for the observation of interesting light-induced states of matter, unless full thermalization is delayed [44, 45], or unless the laser is only

used as a means to break the symmetry for transient intermediate states, such as in the case of laser-controlled novel superconductors [12]. It is therefore an important task to identify material platforms in which crucial energy scales, such as the relevant effective electronic bandwidth, can be tuned with respect to the photon energy of the pump laser. This is exactly the case in twisted van der Waals heterostructures forming Moiré superlattices [46]. In particular, twisted bilayer graphene (TBG) has recently attracted considerable attention due to the discovery of superconductivity [47] along with correlated insulating phases in its vicinity [48]. In TBG, the Fermi velocity and electronic bandwidth of the Dirac bands can be tuned by changing the twisting angle, leading to flat bands at particular magic angles and opening the possibility of *twistronics* [49] and tunable energy absorption spectra [50]. In addition, this paves the way to tune the role of interactions in a materials setting [51], similarly to the case of artificial lattices, in which more exotic Floquet Hamiltonians have been generated [52]. In the context of TBG, this might for instance open the possibility to study strongly correlated Floquet-engineered phases of matter such as the proposed fractional Floquet-Chern insulator [53].

In this work we perform a full tight-binding model calculation for TBG for an intermediate rotation angle, $\Theta = 7.34^\circ$ with a unit cell containing 244 sites, in order to investigate its electronic and topological properties in and out of equilibrium above the magic angle regime in a microscopic picture. A circularly polarized laser field with a frequency of 2.23 eV, tuned to the bandwidth of the lowest energy band manifold, breaks time-reversal symmetry and induces a topologically nontrivial phase, which is tracked by the Berry curvature of Floquet bands projected onto the bare energy eigenstates. We find that the topology of TBG above the magic angles ultimately corresponds to two copies of single-layer graphene. For

* michael.sentef@mpsd.mpg.de

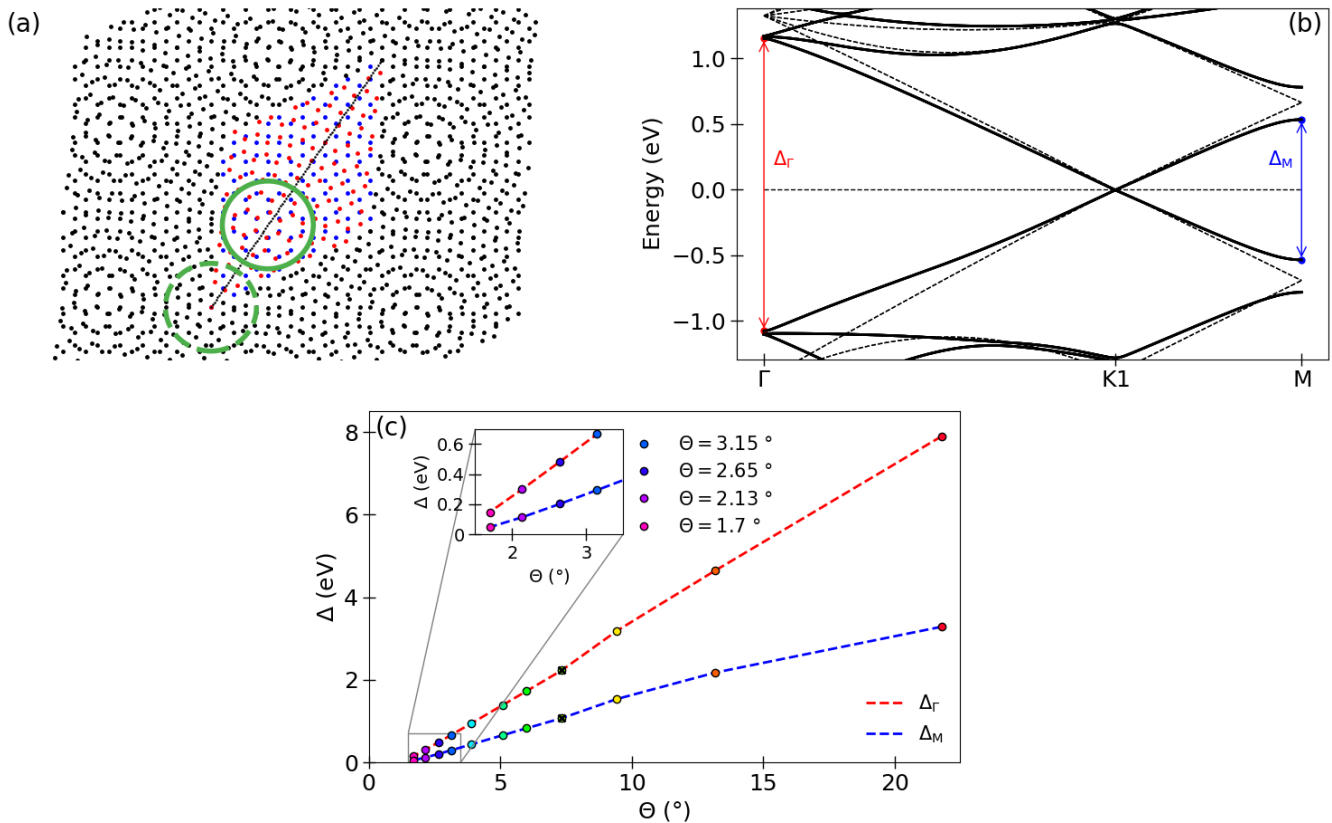


FIG. 1. Atomic structure and tight-binding model bands of equilibrium twisted bilayer graphene. (a) Real-space atomic lattice. Red (blue) points denote the carbon atoms of the bottom (top) layer of one supercell. The black dotted line indicates the mirror-symmetry line which maps the in-plane atomic coordinates of both layers onto each other. The origin is chosen on an AA -stacked carbon site. The twist angle is $\Theta = 7.34^\circ$, which corresponds to a supercell with 244 atoms. The full (dashed) circle indicates a region of A - A (A - B) stacking. (b) Equilibrium band structure along Γ - K_1 - M , where $|\Gamma - K_1| = 0.22 \text{ \AA}^{-1}$. The dashed lines show the single-layer band structure without interlayer coupling but folded back into the reduced zone. The bandwidth at Γ (M) is indicated by a red (blue) arrow. (c) Equilibrium bandwidth of the valence and conduction bands at Γ (red line) and M (blue line) for different twist angles, Θ ($\Theta = 7.34^\circ$ values colored black). The inset shows small angles, whose associated bandwidths lie within the mid-infrared photon energy range.

circularly polarized driving, we find a nontrivial Chern-insulating band structure (with Chern number $C = 4$), while in equilibrium, the system exhibits trivial topology with cancellations of valley Berry curvature when inversion symmetry is broken by a backgate bias voltage between the layers. This offers the unique opportunity, in contrast to single-layer graphene, to study the transition between the topologically trivial and non-trivial phases, as originally envisioned by Haldane in his seminal work on the quantum anomalous Hall effect [54]. Notably this is unlike the case of time-reversal symmetry breaking by a magnetic field, where the large magnetic unit cell and corresponding small Brillouin zone cause dramatically different effects such as the emergence of a Hofstadter butterfly [55]. Our results confirm that for angles larger than the highest magic angle (1.05°) the interlayer interactions can be captured by perturbative treatment, which maintains the linear band dispersions while renormalizing the

Fermi velocities, as stated in [56, 57]. Furthermore, we explicitly show that this is not only true for the electronic band energies but also for the system topology. Thus we expect a time-resolved Hall current measurement, in the time-reversal symmetry-broken state, to show a nonzero Hall conductance [34, 54] approaching a quantized value of $4e^2/h$ for completely filled valence bands and empty conduction bands, where the factor of 4 reflects two valence bands, two spin species, and two valleys.

The paper is organized as follows. In Sec. I, we explain the basic properties of our tight-binding model. In Sec. II, we investigate the electronic properties of our starting point, particularly the equilibrium topology of the system. Sec. III outlines the Floquet electronic band structure and its key differences, compared to equilibrium. In Sec. IV we present our main result of the Floquet engineered Berry curvature and explore the Floquet-topological phase space in dependence of driving ampli-

tudes and different choices of local potentials. We finish by a brief conclusion in Sec. V.

II. TIGHT-BINDING MODEL

Our starting point are two A - A -stacked graphene layers [58]. Choosing the origin of the cartesian coordinate system at an atomic site, we construct the bilayer by a rotation of the top layer by a twist angle, $\Theta = 7.34^\circ$. This rotation amounts to a reflection of the bottom layer within the x - y -plane along the supercell diagonal, as depicted in Fig. 1(a). Using the commensurability condition derived in [56], this results in a supercell of 244 carbon atoms, which has regions of A - A - and A - B -stacking, respectively. We use a general tight-binding hopping Hamiltonian of the form

$$H = \sum_i \epsilon_i c_i^\dagger c_i + \sum_{i \neq j} t_{ij} c_i^\dagger c_j, \quad (1)$$

where c_i^\dagger (c_i) creates (annihilates) an electron in the p_z orbital at the atomic position \mathbf{r}_i . The variables ϵ_i and t_{ij} denote the local potential and hopping matrix elements, respectively. The model parameters are given in Appendix A.

The equilibrium band structure along the symmetry path Γ - K_1 - M in the mini-Brillouin zone (mBZ) of the Moiré superlattice is presented in Fig. 1(b). It shows a linear Dirac-cone dispersion around one Dirac point K_1 with a renormalized Fermi velocity, $v_F/v_F^0 = 0.9$, compared to the one in single-layer graphene (dashed lines). The renormalized Γ -point bandwidth Δ_Γ and M -point energy difference Δ_M for the bottom conduction and top valence bands are indicated by colored arrows.

Envisioning periodic laser driving at specific photon energies with the goal to Floquet-engineer a light-induced anomalous Hall effect [31, 32], we now address the relevant electronic energy scales as a function of twisting angle. To this end we show in Fig. 1(c) both Δ_Γ and Δ_M for different commensurate rotation angles above the magic-angle regime. As discussed in various references, such as 46, the low-energy Dirac bands can be rescaled to exhibit a desired bandwidth by tuning to particular twist angles. In the inset of Fig. 1(c) we focus on the range of angles for which the Δ values lie in the range attainable in an existing ultrafast transport setup [31]. This opens up the possibility of a Floquet-engineered band structure with a light-induced anomalous Hall effect if the laser breaks time-reversal symmetry (see below) with electronic energy scales tunable near the photon energy. This might for instance be possible for a twist angle of 1.7° and photon energy of 200 meV, which matches roughly the low-energy bandwidth in this case.

III. EQUILIBRIUM TOPOLOGY

Before turning to Floquet-engineered bands and topology, we first discuss the equilibrium Berry curvature near the Dirac points when different onsite potentials are applied to TBG. This can be seen as a direct generalization of the Haldane model for single-layer graphene [54] with broken inversion symmetry and intact time-reversal symmetry.

For the onsite potentials we choose from three different options, detailed in Appendix A: (i) a backgate voltage which corresponds to an energetic difference V_{BG} between the top and bottom layers; (ii) an asymmetric A - B potential with energetic difference V_{AB}^{asym} between A and B sublattice in one layer and $-V_{AB}^{\text{asym}}$ in the other layer; and (iii) a symmetric A - B potential with energetic difference V_{AB}^{sym} between A and B sublattice in both layers. As we will see, different combinations of these potentials (i) and (ii) and (i) and (iii), respectively, lead to different band structures and different Berry curvatures within the bands. We notice that for the real TBG device, $V_{AB}^{\text{sym}} = 0$ and $V_{AB}^{\text{asym}} = 0$. These onsite potentials should be seen as fictitious potentials that illustrate how the topology changes for different ways in which inversion symmetry can be broken, similarly in spirit to the Haldane model. However, the backgate potential can be applied experimentally, as has been demonstrated for conventional A - B -stacked bilayer graphene [59, 60]. Unlike the case of A - B -stacked bilayer graphene, which has a parabolic energy dispersion, TBG does have a Dirac-like dispersion, which offers the unique opportunity to experimentally study the competition between broken time-reversal and broken inversion symmetries.

Fig. 2 shows the evolution of band structures and Berry curvatures (see Appendix C) near both Dirac points K_1 and K_2 in the mBZ for twist angle $\Theta = 7.34^\circ$. First we focus on infinitesimally small $V_{AB}^{\text{asym}} = V_{BG} = 0.0001$ eV (Fig. 2(a),(b)). Both the valence and conduction bands are still almost twofold degenerate and a small energy gap of order 0.0001 eV opens at K_1 and K_2 , inducing a nonvanishing Berry curvature. Fig. 2(b) shows the Berry curvature in the two valence bands. For one valence band (green solid line) the Berry curvature is negative at K_1 and positive at K_2 , while it is exactly the opposite for the other valence band (purple dashed line). Thus the Berry curvature integrated within each valley (K_1 and K_2) vanishes. The same qualitative behavior is observed for increased values of the asymmetric potential $V_{AB}^{\text{asym}} = 0.01$ eV larger than the backgate potential $V_{BG} = 0.001$ eV (Fig. 2(e),(f)) as well as asymmetric potential $V_{AB}^{\text{asym}} = 0.01$ eV smaller than the backgate potential $V_{BG} = 0.05$ eV (Fig. 2(i),(j)). In these cases the Berry curvature is spread out a bit more in momentum space. In the latter case with larger backgate potential one can observe additional band crossings to the left and right of the Dirac points (Fig. 2(i)) with vanishing Berry curvature (Fig. 2(j)).

We now study what happens for the case of a sym-

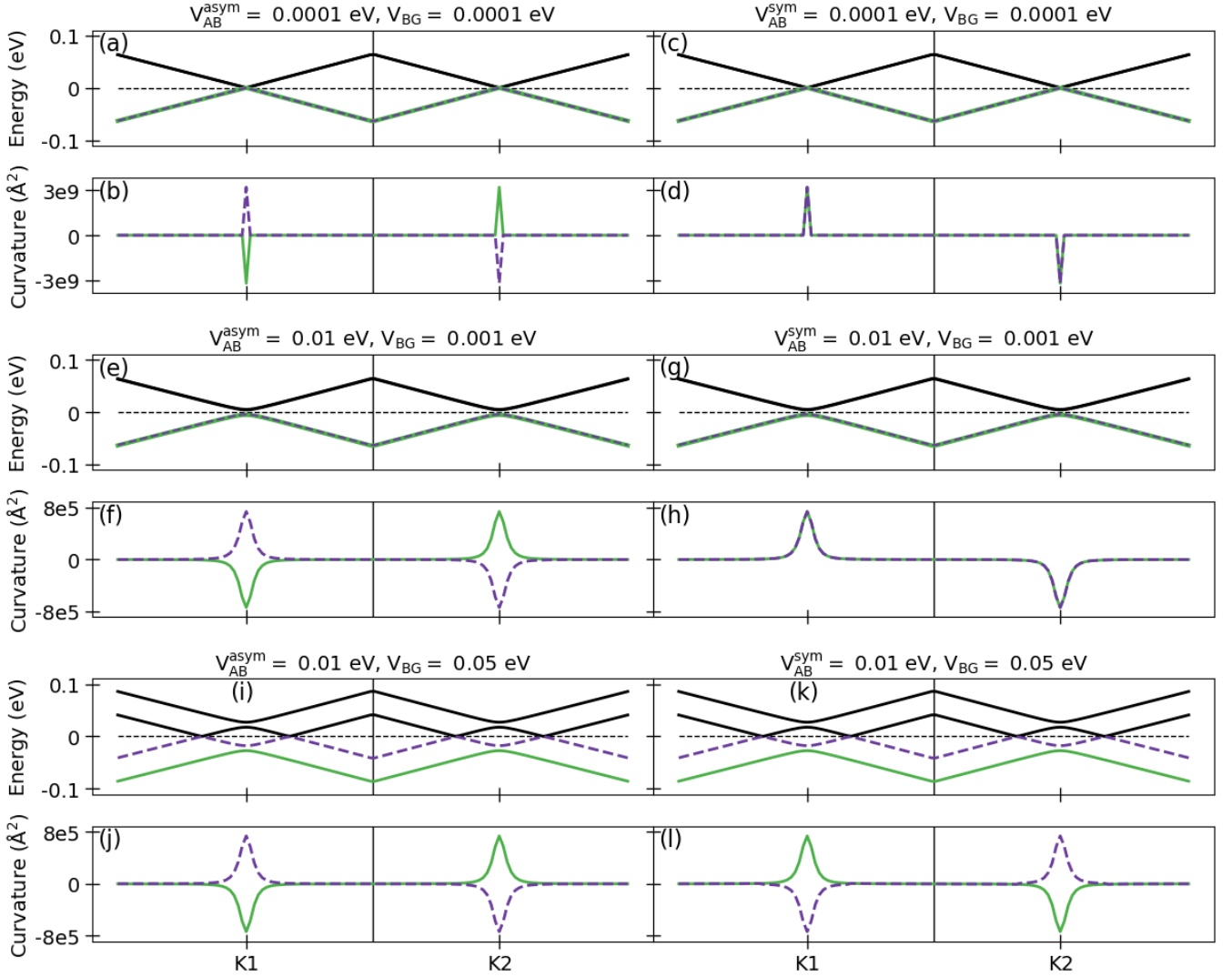


FIG. 2. Equilibrium band structure and corresponding valence-band Berry curvatures in close proximity to the Dirac points of the mBZ along Γ - K_1 - M - K_2 - Γ (interval of length 0.022 \AA^{-1} around K_1 and K_2) for different onsite potentials V_{AB} and backgate voltages V_{BG} . (a),(c),(e) Antisymmetric \pm/\mp sublattice potential within the layers. (g),(i),(l) Symmetric \pm/\pm sublattice potentials. (b),(f),(j),(l) Local and valley band curvature shows opposite sign, respectively. (d),(h) Non-vanishing valley Berry curvature but zero integrated Berry curvature due to sign flip between valleys.

metric A - B potential V_{AB}^{sym} . For infinitesimally small potentials $V_{AB}^{\text{sym}} = V_{BG} = 0.0001 \text{ eV}$ (Fig. 2(c),(d)) both valence bands show the same Berry curvature being positive near K_1 and negative near K_2 . Thus in the symmetric case, as opposed to the asymmetric case, there is a non-vanishing total valley Berry curvature but vanishing overall Berry curvature due to cancellation between both valleys in the mBZ. The same qualitative behavior is observed for increased values of the symmetric potential $V_{AB}^{\text{sym}} = 0.01 \text{ eV}$ larger than the backgate potential $V_{BG} = 0.001 \text{ eV}$ (Fig. 2(g),(h)). This behavior is switched when the backgate potential $V_{BG} = 0.05 \text{ eV}$ is larger than the symmetric potential $V_{AB}^{\text{sym}} = 0.01 \text{ eV}$ (Fig. 2(k),(l)). In this case the Berry curvature is analogous to the one for the asymmetric case with vanishing valley Berry curva-

ture for each valley individually. This finding is particularly interesting as it opens up the possibility of starting from a topologically trivial insulating phase for $V_{BG} \neq 0$ and $V_{AB} = 0$, which is the realistic scenario for TBG. Below we will show that by applying circularly polarized light, one can light-induce the transition from topologically trivial to topologically nontrivial insulating band structures at a nonvanishing critical field strength, which is not possible for single-layer graphene.

Overall we note that TBG obviously offers more possibilities for combinations of Berry curvature than single-layer graphene. In particular the Berry curvature can vanish per valley when summed over all valence bands, while being nonzero for each band separately within a valley, for broken inversion symmetry due to an asymmetric

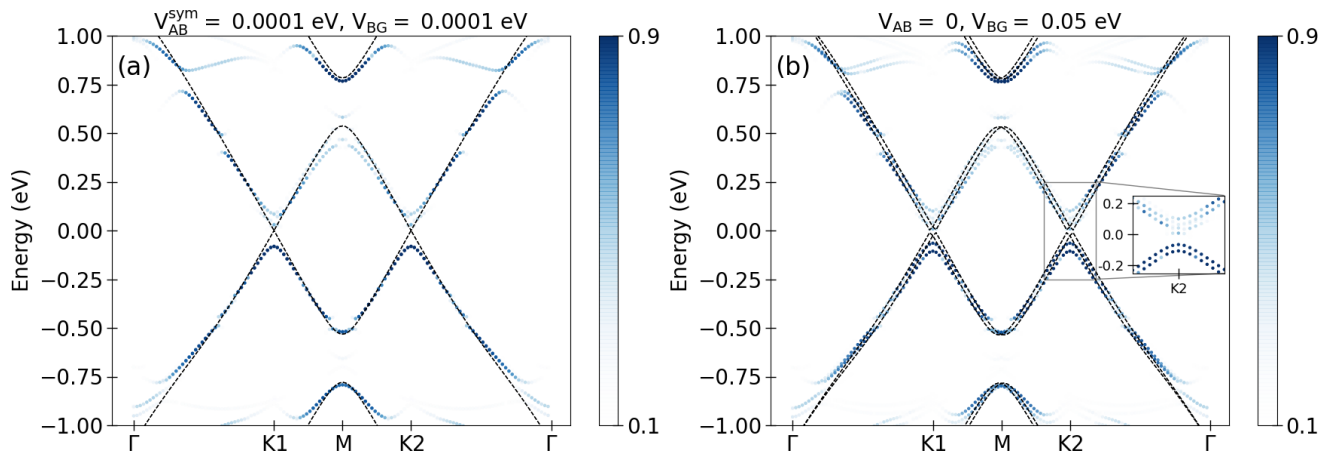


FIG. 3. Floquet band structures for a strong circularly polarized driving field with $E_{max} = 13.7$ MV/cm ($A = 0.15 \text{ \AA}^{-1}$ at $\Omega = 2.23$ eV) for different onsite potentials V_{AB} and backgate voltages V_{BG} . The black dashed lines indicate the equilibrium bare bands. The overlap between the Floquet bands and the equilibrium bare bands is denoted by the blue color as indicated in the color bars. In both cases the breaking of time-reversal symmetry adds mass to the Dirac bands, which results in a finite energy gap at the Dirac points. Additionally, gaps open away from the Dirac points, due to resonant coupling between Floquet bands. The inset in (b) shows a close-up of the region near K_2 .

A - B potential or due to a symmetric A - B potential when the backgate voltage exceeds this A - B potential. This scenario obviously does not exist for single-layer graphene which has only one valence band (per spin, which is suppressed here) in the Dirac bands. In all cases discussed here the total Berry curvature and thus the valence band Chern number vanishes when time-reversal symmetry is intact, like in single-layer graphene or the Haldane model with time-reversal symmetry. Importantly, we do not make a claim about the topology of the regime at and below the highest magic angle around 1.05° , for which there have been several predictions for the effective Berryology [61–64].

IV. FLOQUET BAND STRUCTURE

We now turn to the case of laser-driven TBG with circularly polarized light in which Floquet bands are formed. Focusing again on a twist angle $\Theta = 7.34^\circ$, used here and in all that follows, we choose a photon frequency $\Omega = 2.23$ eV tuned to the bandwidth Δ_Γ for this particular twist angle. This choice is motivated by the fact that Floquet sidebands overlapping with the original bands are not created in this case within the low-energy Dirac bands, but only with higher lying bands. The laser field is described by a time-dependent, spatially homogeneous vector potential $\mathbf{A}(t) = A_{max}(\mathbf{e}_x \sin(\Omega t) + \mathbf{e}_y \cos(\Omega t))$, and is coupled to the electrons in TBG via Peierls substitution,

$$t_{ij} \rightarrow \tilde{t}_{ij}(t) = t_{ij} e^{i\mathbf{A}(t) \cdot \mathbf{r}_{ij}}. \quad (2)$$

From the resulting time-dependent Hamiltonian we compute the Floquet bands by expanding in Floquet harmonics [65–67] and diagonalizing the Floquet Hamiltonian

with a cutoff in the Floquet index and checked convergence in this cutoff. In order to plot the resulting bands and their topology we choose to project the Floquet bands onto the original energy eigenstates of the bare Hamiltonian, i.e., to compute the square of the wavefunction overlap and color the resulting Floquet bands with a color scale according to this overlap (see Sec. B).

In Fig. 3 we show the original equilibrium bands (dashed lines) and the projected Floquet bands for a relatively strong laser field ($E_{max} = 13.7$ MV/cm) and two cases, the one of infinitesimal potentials $V_{AB}^{sym} = V_{BG} = 0.0001$ eV (Fig. 3(a)) and the one of vanishing A - B potential but nonvanishing backgate potential $V_{BG} = 0.05$ eV (Fig. 3(b)). For the case in Fig. 3(a) the bare bands correspond essentially to the Dirac bands of pristine TBG. The circularly polarized driving field opens a sizeable energy gap at both Dirac points K_1 and K_2 and creates a variety of Floquet bands, most of them with relatively small overlap with the equilibrium bands. Nevertheless a number of avoided band crossings are visible in the chosen energy window, leading to a more complicated structure than for single-layer graphene. Similarly, for the case in Fig. 3(b) the main feature induced by the laser driving is a band gap opening at K_1 and K_2 but now with visibly split Floquet valence and conduction bands due to the sizeable backgate potential.

V. FLOQUET-ENGINEERED TOPOLOGY

Finally, the obvious follow-up question to address is the one of the light-induced Berry curvature and corresponding Floquet-band topology. To this end we focus on the low-energy Floquet-Dirac bands near K_1 and K_2 and color these bands according to their respective Berry cur-

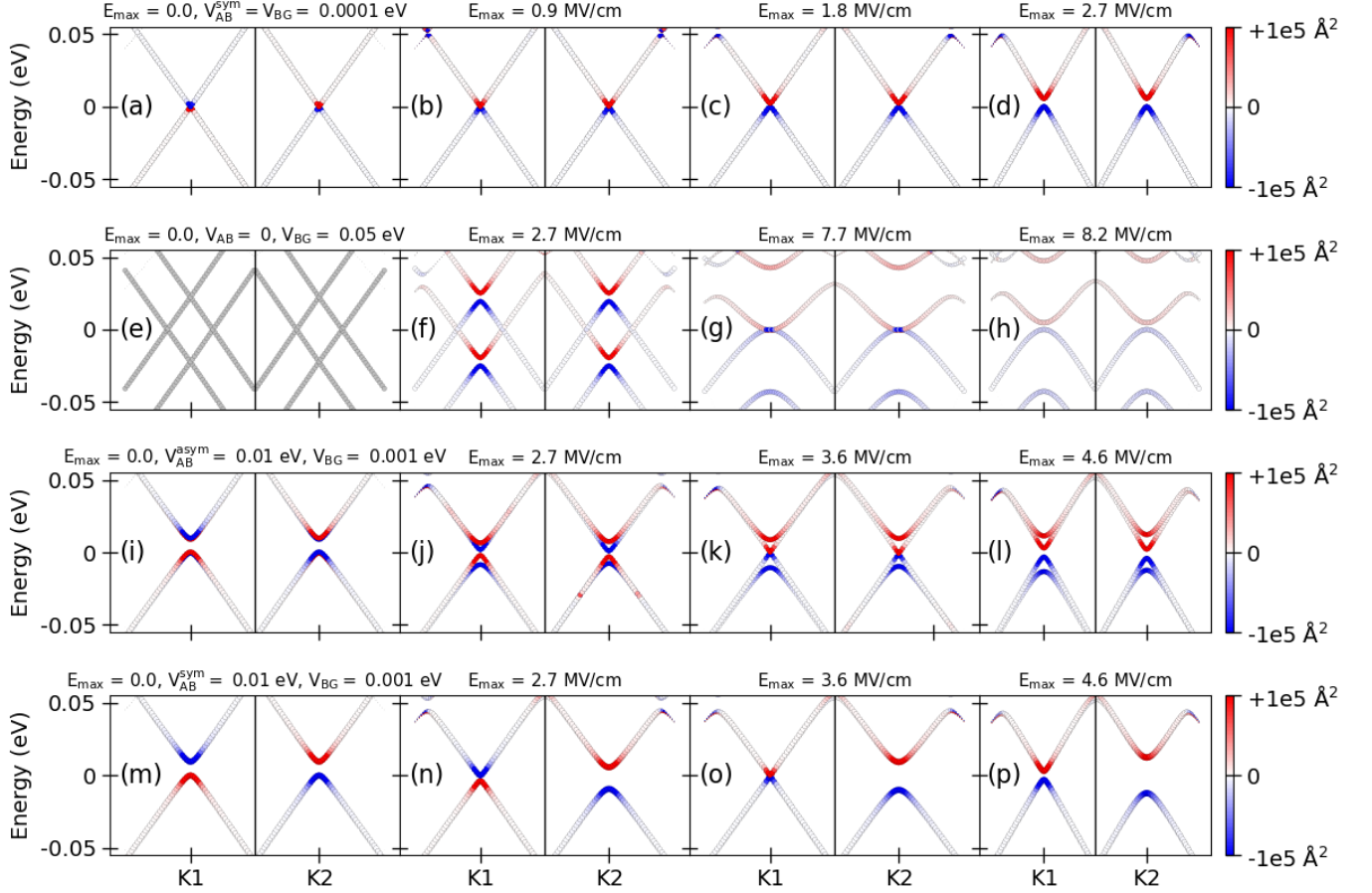


FIG. 4. Floquet-engineered Berry curvature near the two Dirac points of the mBZ along Γ - K_1 - M - K_2 - Γ for different onsite potentials V_{AB} , backgate voltages V_{BG} , and increasing circularly polarized field amplitudes E_{max} . The size of the points indicate the overlap with the original equilibrium bands. Throughout, $\Delta_{\Gamma} = 2.23$ eV is chosen as Floquet driving frequency. (a),(e),(i),(m) Equilibrium case. In (e) the Berry curvature is not defined at K_1 (K_2), due to band degeneracy, and zero otherwise. (b) For infinitesimally small potentials, a finite driving amplitude immediately opens a gap and induces a nontrivial Floquet-band topology. (f),(i),(j),(m),(n) Topologically trivial phase, characterized by zero integrated Berry curvature of the valence (conduction) bands. (g),(k),(o) Topological transition indicated by gap closing. (g) Trivial shift of bands while the sign of associated Berry curvature is preserved. (k) Gap closing and flow of Berry curvature between lowermost conduction band and uppermost valence band. (o) Gap closing and flow of Berry curvature both between bottom conduction band and valence band and between top conduction band and valence band, respectively. (b),(c),(d),(h),(i),(p) Chern-insulating phase, characterized by re-opened gaps and a finite integrated Berry curvature in the valence (conduction) bands.

vatures. The resulting Floquet-engineered Berry curvatures are presented in Fig. 4. Fig. 4(a)-(d) shows the evolution for infinitesimal potentials $V_{AB}^{sym} = V_{BG} = 0.0001$ eV as a function of increasing driving field strength E_{max} . Initially in equilibrium (Fig. 4(a)) one observes a nonzero Berry curvature in each valley but with flipped sign between valleys (cf. Fig. 2(d)). This immediately changes when a driving field is applied (Fig. 4(b)), which leads to a band inversion and sign change of the Berry curvature around K_1 and a non-vanishing total Berry curvature in the valence bands (conduction bands) due to broken time-reversal symmetry exceeding the breaking of inversion symmetry. Similarly to the Haldane model case in the high-frequency driving limit, this is then expected to lead to an almost quantized light-induced anomalous

Hall effect but with an additional double degeneracy due to the bilayer instead of single-layer structure ($4e^2/h$ instead of $2e^2/h$). The observed band gap and spreading of the Berry curvature in momentum space become more pronounced as the field strength increases (Fig. 4(c),(d)).

We now turn to the case of vanishing A-B potential and nonzero backgate potential $V_{BG} = 0.05$ eV (Fig. 4(e)-(h)). Initially the Berry curvature vanishes identically everywhere (Fig. 4(e)). Turning on the laser field, a nonvanishing Berry curvature is induced but with compensation between the two valence bands (conduction bands) for a moderate field (Fig. 4(f)). Increasing the field strength more one reaches a critical field (Fig. 4(g)) at which the top valence band and bottom conduction band invert and the net valence band Berry curvature as well as the net

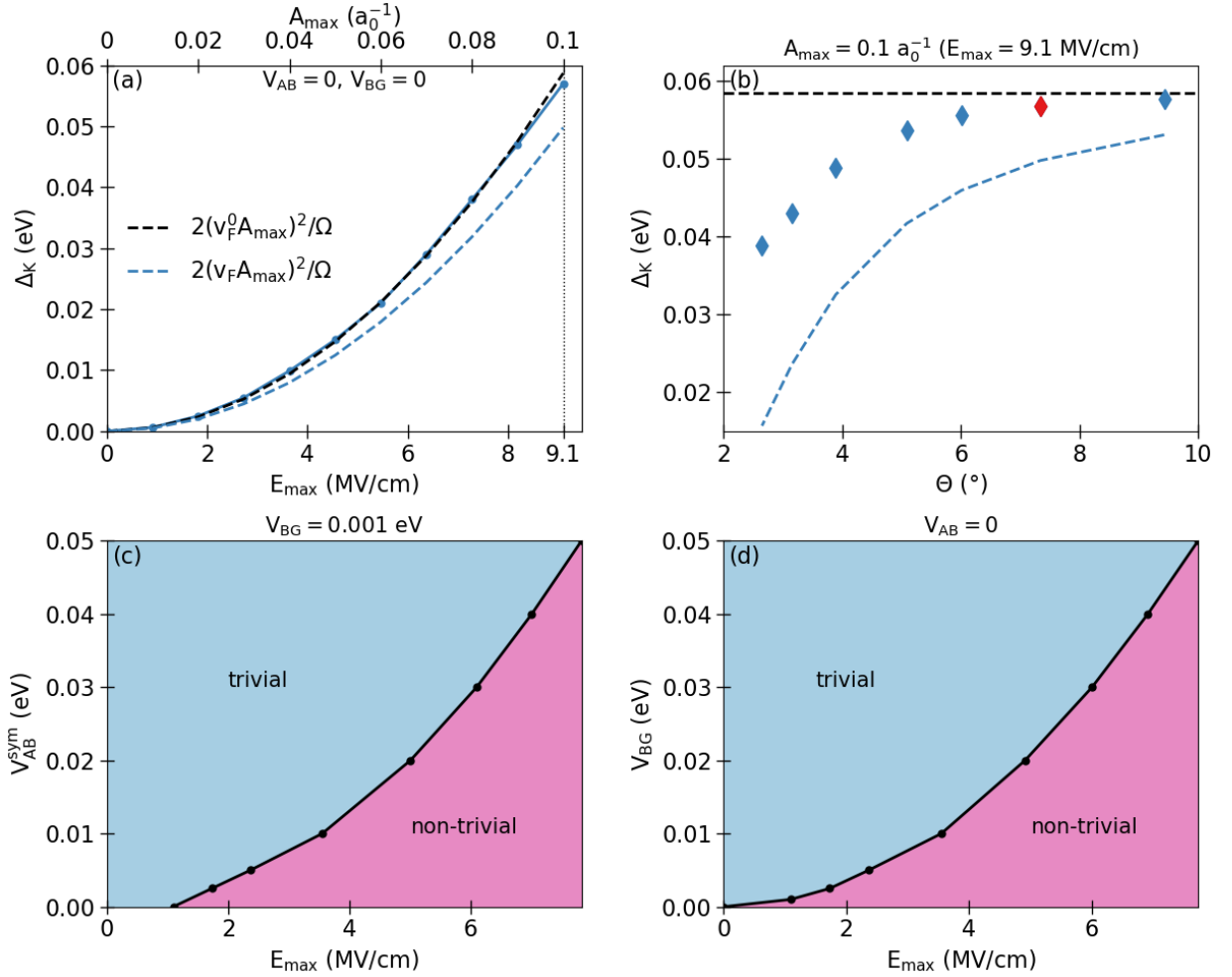


FIG. 5. Floquet topological gaps and phase diagrams. (a) Energy gap at K as a function of the driving field amplitude. The blue (black) dashed line shows the quadratic dependence of the gap on the driving amplitude, A_{\max} , and the equilibrium TBG (monolayer graphene) Fermi velocity, v_F (v_F^0), in the low-amplitude, high-frequency limit. The black dotted line indicates the field strength chosen in panel (b). (b) Energy gap as a function of twist angle for a fixed field strength. The value used throughout the paper, $\Theta = 7.34^\circ$, is indicated by red color. The black dashed line indicates the corresponding single-layer Floquet band gap. The blue dashed line shows the gap values which would be naively expected from the renormalized Fermi velocity. (c),(d) The pink (light blue) area indicates the topologically nontrivial (trivial) phase. (c) With symmetric sublattice potential and small backgate voltage. Due to the additional backgate voltage, the topologically nontrivial phase always requires nonzero driving amplitude. (d) With backgate voltage only. Throughout, a photon frequency, $\Omega = 2.23$ eV, is assumed.

conduction band Berry curvature become nonzero. This topological phase transition is completed at even larger field strength (Fig. 4(h)).

A topological Floquet-engineered phase transition is induced at smaller field strength when the backgate voltage is smaller, $V_{BG} = 0.001$ eV (Fig. 4(i)-(l)), where we also include an asymmetric A - B potential $V_{AB}^{\text{asym}} = 0.01$ eV larger than the backgate potential. This is the same as the scenario discussed before where the valley Berry curvature vanishes when integrated over all valence bands in the absence of the laser field. This is changed by the laser driving and a band inversion and flow of Berry curvature between top valence and bottom conduction bands is observed simultaneously in both valleys at a critical field

strength (Fig. 4(k)).

By contrast, for $V_{BG} = 0.001$ eV and a larger symmetric onsite potential $V_{AB}^{\text{sym}} = 0.01$ eV (Fig. 4(m)-(p)), we have a net nonzero valley Berry curvature (Fig. 4(m)), qualitatively equivalently to the case of the single-layer Haldane model. In this case a moderate driving field creates asymmetric energy gaps at K_1 versus K_2 (Fig. 4(n)), where one of the gaps at K_2 increases due to the laser, while the other one at K_1 decreases. A gap closing and band inversion is then observed at K_1 for a critical field strength (Fig. 4(o)) with a completed transition to a topological Chern-insulating Floquet band structure above the critical field strength ((Fig. 4(p))).

We note that these Floquet-engineered Berry curva-

tures could be measured in a momentum-, energy- and time-resolved fashion using circularly polarized time- and angle-resolved photoemission spectroscopy [68]. Finally, we summarize our findings for the Floquet-engineered band gaps and topology in Fig. 5. Fig. 5(a) shows the Dirac point band gap at zero onsite potentials (pristine TBG) as a function of laser driving field strength, or as a function of peak vector potential, respectively. The blue (black) dashed line shows $2(v_F A_{\max})^2/\Omega$ ($2(v_F^0 A_{\max})^2/\Omega$), respectively, with v_F the renormalized Fermi velocity of TBG and v_F^0 the bare Fermi velocity of single-layer graphene. Interestingly, the light-induced band gap scales essentially with the bare Fermi velocity of single-layer graphene as opposed to the renormalized one in TBG (see Appendix for an extended discussion). For small twist angles, however, deviations from scaling with v_F^0 appear. The origin of this scaling behavior presumably lies in the fact that the renormalization of the Fermi velocity stems from interlayer hoppings, which are predominantly perpendicular to the plane of the individual graphene layers. In contrast, the light field is chosen to have in-plane polarization, thus not coupling to the out-of-plane currents. Therefore, the single-layer Fermi velocity is the key ingredient for the light-induced band gap.

Fig. 5(b) shows the Floquet band gap at the Dirac points for vanishing onsite potentials at different intermediate twist angles. The peak electric field strength, $E_{\max} = 9.1$ MV/cm, and the driving frequency, $\Omega = 2.23$ eV, are kept constant. The gap increases as a function of twist angle at small twist angles and then reaches a plateau approaching the gap value for single-layer graphene. Clearly, for 7.34° the size of the gap is very close to the single-layer value. [69]

Fig. 5(c) shows the Floquet phase diagram with the trivial phase (vanishing valence band integrated Berry curvature) and nontrivial phases (non-zero integrated Berry curvature) as a function of field strength for varying symmetric A - B potential and a small backgate voltage. Due to the backgate voltage, as seen already in Fig. 4, a finite critical field strength is required to switch the system to the topologically nontrivial phase. This changes in the case of a vanishing A - B potential and a finite backgate voltage, shown in Fig. 5(d). Here, essentially the shape of the phase boundary exhibits the same quadratic dependence on field strength as the energy gap in Fig. 5(a).

CONCLUSION AND OUTLOOK

We have shown how the Berry curvature in twisted bilayer graphene is affected by different types of inversion-symmetry breaking. The effects of circularly polarized light on the full tight-binding model of twisted bilayer graphene are found to be essentially as expected for two copies of single-layer graphene. Importantly, the light-induced energy gap is not strongly affected by interlayer

coupling at twist angles much larger than the largest magic angle. Moreover, the opportunity to break inversion symmetry by backgating allows to tune the phase transition between topologically trivial and nontrivial states, in distinct contrast with single-layer graphene. This opens up the realistic prospect of a finite-field topological transition in solid-state experiments. A future task is to study theoretically the ultrafast light-induced transport properties of TBG for realistic driving pulses especially in the mid-infrared and for smaller twisting angles near 1.7° , including the effects of excitation and dissipation in real time, which is a much more formidable task for TBG compared to a single branch of Dirac fermions [32, 33]. In particular, real-time signatures of tunneling into topological edge states might provide additional insights [70]. An intriguing opportunity opens up for small twist angles, at which the distance between both Dirac points in the mini-Brillouin zone becomes very small. In this case, the laser field strength could realistically lead to a peak vector potential that exceeds the distance $|K_2 - K_1|$. In this case the band gap induced initially by a moderate field amplitude could close again leading to a second topological phase transition, which should lead to a signature in the Hall transport experiment. Moreover it is also interesting to address the question of light-induced topology without classical driving fields by encapsulating TBG in a cavity, as recently proposed for single-layer graphene [71].

Finally the possibility to not only tune single-particle bandwidth and Berry curvature but also interaction effects [51, 53] could pave the way for solid-state platforms with exotic nonequilibrium phases of matter analogous to Floquet-engineered interaction phases in artificial lattices [52]. Moreover, the concept of twistrionics can also be extended to other two-dimensional materials, such as hexagonal boron nitride [72] and GeSe [73], and it is an intriguing subject for future study to investigate Floquet engineering in these materials.

ACKNOWLEDGEMENT

Discussions with S. A. Sato are gratefully acknowledged. G.E.T. and M.A.S. acknowledge financial support by the DFG through the Emmy Noether program (SE 2558/2-1). This work was supported by the European Research Council (ERC-2015-AdG694097). The Flatiron Institute is a division of the Simons Foundation.

VI. BIBLIOGRAPHY

- [1] D. N. Basov, R. D. Averitt, and D. Hsieh, "Towards properties on demand in quantum materials," *Nature Materials* **16**, 1077 (2017).
- [2] Thomas W. Ebbesen, "Hybrid Light-Matter States in a Molecular and Material Science Perspective," *Acc. Chem. Res.* **49**, 2403-2412 (2016).

- [3] Johannes Flick, Michael Ruggenthaler, Heiko Appel, and Angel Rubio, “Atoms and molecules in cavities, from weak to strong coupling in quantum-electrodynamics (QED) chemistry,” *PNAS* **114**, 3026–3034 (2017).
- [4] Johannes Flick, Nicholas Rivera, and Prineha Narang, “Strong light-matter coupling in quantum chemistry and quantum photonics,” *Nanophotonics* **7**, 1479–1501 (2018).
- [5] Michael Ruggenthaler, Nicolas Tancogne-Dejean, Johannes Flick, Heiko Appel, and Angel Rubio, “From a quantum-electrodynamical light-matter description to novel spectroscopies,” *Nature Reviews Chemistry* **2**, 0118 (2018).
- [6] Christian Schäfer, Michael Ruggenthaler, Heiko Appel, and Angel Rubio, “Modification of excitation and charge transfer in cavity quantum-electrodynamical chemistry,” *PNAS* **116**, 4883–4892 (2019).
- [7] Andreas Hemmerich, “Effective time-independent description of optical lattices with periodic driving,” *Phys. Rev. A* **81**, 063626 (2010).
- [8] Marin Bukov, Luca D’Alessio, and Anatoli Polkovnikov, “Universal high-frequency behavior of periodically driven systems: from dynamical stabilization to Floquet engineering,” *Advances in Physics* **64**, 139–226 (2015).
- [9] André Eckardt, “Colloquium: Atomic quantum gases in periodically driven optical lattices,” *Rev. Mod. Phys.* **89**, 011004 (2017).
- [10] Matteo Rini, Ra’anan Tobey, Nicky Dean, Jiro Itatani, Yasuhide Tomioka, Yoshinori Tokura, Robert W. Schoenlein, and Andrea Cavalleri, “Control of the electronic phase of the manganite by mode-selective vibrational excitation,” *Nature* **449**, 72–74 (2007).
- [11] L. Stojchevska, I. Vaskivskiy, T. Mertelj, P. Kusar, D. Svetin, S. Brazovskii, and D. Mihailovic, “Ultrafast Switching to a Stable Hidden Quantum State in an Electronic Crystal,” *Science* **344**, 177–180 (2014).
- [12] M. Claassen, D. M. Kennes, M. Zingl, M. A. Sentef, and A. Rubio, “Universal optical control of chiral superconductors and Majorana modes,” *Nature Physics*, **1** (2019), arXiv:1810.06536.
- [13] R. Singla, G. Cotugno, S. Kaiser, M. Först, M. Mitrano, H. Y. Liu, A. Cartella, C. Manzoni, H. Okamoto, T. Hasegawa, S. R. Clark, D. Jaksch, and A. Cavalleri, “THz-Frequency Modulation of the Hubbard U in an Organic Mott Insulator,” *Physical Review Letters* **115** (2015), 10.1103/PhysRevLett.115.187401, arXiv:1409.1088.
- [14] E. Pomarico, M. Mitrano, H. Bromberger, M. A. Sentef, A. Al-Temimy, C. Coletti, A. Stöhr, S. Link, U. Starke, C. Cacho, R. Chapman, E. Springate, A. Cavalleri, and I. Gierz, “Enhanced electron-phonon coupling in graphene with periodically distorted lattice,” *Phys. Rev. B* **95**, 024304 (2017).
- [15] Nicolas Tancogne-Dejean, Michael A. Sentef, and Angel Rubio, “Ultrafast Modification of Hubbard U in a Strongly Correlated Material: Ab initio High-Harmonic Generation in NiO,” *Phys. Rev. Lett.* **121**, 097402 (2018).
- [16] D. Fausti, R. I. Tobey, N. Dean, S. Kaiser, A. Dienst, M. C. Hoffmann, S. Pyon, T. Takayama, H. Takagi, and A. Cavalleri, “Light-Induced Superconductivity in a Stripe-Ordered Cuprate,” *Science* **331**, 189–191 (2011).
- [17] M. Mitrano, A. Cantaluppi, D. Nicoletti, S. Kaiser, A. Perucchi, S. Lupi, P. Di Pietro, D. Pontiroli, M. Riccò, S. R. Clark, D. Jaksch, and A. Cavalleri, “Possible light-induced superconductivity in K3c60 at high temperature,” *Nature* **530**, 461–464 (2016).
- [18] E. Orgiu, J. George, J. A. Hutchison, E. Devaux, J. F. Dayen, B. Doudin, F. Stellacci, C. Genet, J. Schachenmayer, C. Genes, G. Pupillo, P. Samorì, and T. W. Ebbesen, “Conductivity in organic semiconductors hybridized with the vacuum field,” *Nat Mater* **14**, 1123–1129 (2015).
- [19] M. A. Sentef, M. Ruggenthaler, and A. Rubio, “Cavity quantum-electrodynamical polaritonically enhanced electron-phonon coupling and its influence on superconductivity,” *Science Advances* **4**, eaau6969 (2018).
- [20] Giacomo Mazza and Antoine Georges, “Superradiant Quantum Materials,” *Phys. Rev. Lett.* **122**, 017401 (2019).
- [21] Jonathan B. Curtis, Zachary M. Raines, Andrew A. Alloca, Mohammad Hafezi, and Victor M. Galitski, “Cavity Quantum Eliashberg Enhancement of Superconductivity,” *Phys. Rev. Lett.* **122**, 167002 (2019).
- [22] Martin Kiffner, Jonathan R. Coulthard, Frank Schlawin, Arzhang Ardavan, and Dieter Jaksch, “Manipulating quantum materials with quantum light,” *Phys. Rev. B* **99**, 085116 (2019).
- [23] Raphael F. Ribeiro, Luis A. Martínez-Martínez, Matthew Du, Jorge Campos-Gonzalez-Angulo, and Joel Yuen-Zhou, “Polariton chemistry: controlling molecular dynamics with optical cavities,” *Chem. Sci.* **9**, 6325–6339 (2018).
- [24] Alessandro Zenesini, Hans Lignier, Donatella Ciampini, Oliver Morsch, and Ennio Arimondo, “Coherent Control of Dressed Matter Waves,” *Phys. Rev. Lett.* **102**, 100403 (2009).
- [25] J. Struck, C. Ölschläger, R. Le Targat, P. Soltan-Panahi, A. Eckardt, M. Lewenstein, P. Windpassinger, and K. Sengstock, “Quantum Simulation of Frustrated Classical Magnetism in Triangular Optical Lattices,” *Science* **333**, 996–999 (2011).
- [26] M. Aidelsburger, M. Atala, S. Nascimbène, S. Trotzky, Y.-A. Chen, and I. Bloch, “Experimental Realization of Strong Effective Magnetic Fields in an Optical Lattice,” *Phys. Rev. Lett.* **107**, 255301 (2011).
- [27] Gregor Jotzu, Michael Messer, Rémi Desbuquois, Martin Lebrat, Thomas Uehlinger, Daniel Greif, and Tilman Esslinger, “Experimental realization of the topological Haldane model with ultracold fermions,” *Nature* **515**, 237–240 (2014).
- [28] Colin J. Kennedy, William Cody Burton, Woo Chang Chung, and Wolfgang Ketterle, “Observation of Bose-Einstein condensation in a strong synthetic magnetic field,” *Nature Physics* **11**, 859–864 (2015).
- [29] Mikael C. Rechtsman, Julia M. Zeuner, Yonatan Plotnik, Yaakov Lumer, Daniel Podolsky, Felix Dreisow, Stefan Nolte, Mordechai Segev, and Alexander Szameit, “Photonic Floquet topological insulators,” *Nature* **496**, 196–200 (2013).
- [30] Y. H. Wang, H. Steinberg, P. Jarillo-Herrero, and N. Gedik, “Observation of Floquet-Bloch States on the Surface of a Topological Insulator,” *Science* **342**, 453–457 (2013).
- [31] J. W. McIver, B. Schulte, F.-U. Stein, T. Matsuyama, G. Jotzu, G. Meier, and A. Cavalleri, “Light-induced anomalous Hall effect in graphene,” *arXiv:1811.03522 [cond-mat]* (2018), arXiv: 1811.03522.

- [32] S. A. Sato, J. W. McIver, M. Nuske, P. Tang, G. Jotzu, B. Schulte, H. Hübener, U. De Giovannini, L. Mathey, M. A. Sentef, A. Cavalleri, and A. Rubio, “Microscopic theory for the light-induced anomalous Hall effect in graphene,” *Phys. Rev. B* **99**, 214302 (2019).
- [33] S. A. Sato, P. Tang, M. A. Sentef, U. De Giovannini, H. Hübener, and A. Rubio, “Light-induced anomalous Hall effect in massless Dirac fermion systems and topological insulators with dissipation,” [arXiv:1905.12981 \[cond-mat, physics:physics\]](https://arxiv.org/abs/1905.12981) (2019), arXiv: 1905.12981.
- [34] Takashi Oka and Hideo Aoki, “Photovoltaic Hall effect in graphene,” *Phys. Rev. B* **79**, 081406 (2009).
- [35] Takuya Kitagawa, Takashi Oka, Arne Brataas, Liang Fu, and Eugene Demler, “Transport properties of nonequilibrium systems under the application of light: Photoinduced quantum Hall insulators without Landau levels,” *Phys. Rev. B* **84**, 235108 (2011).
- [36] Netanel H. Lindner, Gil Refael, and Victor Galitski, “Floquet topological insulator in semiconductor quantum wells,” *Nat Phys* **7**, 490–495 (2011).
- [37] Mark S. Rudner, Netanel H. Lindner, Erez Berg, and Michael Levin, “Anomalous Edge States and the Bulk-Edge Correspondence for Periodically Driven Two-Dimensional Systems,” *Phys. Rev. X* **3**, 031005 (2013).
- [38] Gonzalo Usaj, P. M. Perez-Piskunow, L. E. F. Foa Torres, and C. A. Balseiro, “Irradiated graphene as a tunable Floquet topological insulator,” *Phys. Rev. B* **90**, 115423 (2014).
- [39] L. E. F. Foa Torres, P. M. Perez-Piskunow, C. A. Balseiro, and Gonzalo Usaj, “Multiterminal Conductance of a Floquet Topological Insulator,” *Phys. Rev. Lett.* **113**, 266801 (2014).
- [40] M. A. Sentef, M. Claassen, A. F. Kemper, B. Moritz, T. Oka, J. K. Freericks, and T. P. Devereaux, “Theory of Floquet band formation and local pseudospin textures in pump-probe photoemission of graphene,” *Nature Communications* **6**, 7047 (2015).
- [41] Takahiro Mikami, Sota Kitamura, Kenji Yasuda, Naoto Tsuji, Takashi Oka, and Hideo Aoki, “Brillouin-Wigner theory for high-frequency expansion in periodically driven systems: Application to Floquet topological insulators,” *Physical Review B* **93** (2016), 10.1103/PhysRevB.93.144307, arXiv: 1511.00755.
- [42] Hossein Dehghani, Takashi Oka, and Aditi Mitra, “Out-of-equilibrium electrons and the Hall conductance of a Floquet topological insulator,” *Phys. Rev. B* **91**, 155422 (2015).
- [43] Hannes Hübener, Michael A. Sentef, Umberto De Giovannini, Alexander F. Kemper, and Angel Rubio, “Creating stable Floquet–Weyl semimetals by laser-driving of 3d Dirac materials,” *Nature Communications* **8**, 13940 (2017).
- [44] Dmitry Abanin, Wojciech De Roeck, Wen Wei Ho, and François Huveneers, “A Rigorous Theory of Many-Body Prethermalization for Periodically Driven and Closed Quantum Systems,” *Commun. Math. Phys.* **354**, 809–827 (2017).
- [45] Gabriel E. Topp, Nicolas Tancogne-Dejean, Alexander F. Kemper, Angel Rubio, and Michael A. Sentef, “All-optical nonequilibrium pathway to stabilising magnetic Weyl semimetals in pyrochlore iridates,” *Nature Communications* **9**, 4452 (2018).
- [46] Rafi Bistritzer and Allan H. MacDonald, “Moiré bands in twisted double-layer graphene,” *PNAS* **108**, 12233–12237 (2011).
- [47] Yuan Cao, Valla Fatemi, Shiang Fang, Kenji Watanabe, Takashi Taniguchi, Efthimios Kaxiras, and Pablo Jarillo-Herrero, “Unconventional superconductivity in magic-angle graphene superlattices,” *Nature* **556**, 43–50 (2018).
- [48] Yuan Cao, Valla Fatemi, Ahmet Demir, Shiang Fang, Spencer L. Tomarken, Jason Y. Luo, Javier D. Sanchez-Yamagishi, Kenji Watanabe, Takashi Taniguchi, Efthimios Kaxiras, Ray C. Ashoori, and Pablo Jarillo-Herrero, “Correlated insulator behaviour at half-filling in magic-angle graphene superlattices,” *Nature* **556**, 80–84 (2018).
- [49] Rebeca Ribeiro-Palau, Changjian Zhang, Kenji Watanabe, Takashi Taniguchi, James Hone, and Cory R. Dean, “Twistable electronics with dynamically rotatable heterostructures,” *Science* **361**, 690–693 (2018).
- [50] Pilkyung Moon and Mikito Koshino, “Energy spectrum and quantum Hall effect in twisted bilayer graphene,” *Phys. Rev. B* **85**, 195458 (2012).
- [51] T. M. R. Wolf, J. L. Lado, G. Blatter, and O. Zeitler, “Electrically-tunable flat bands and magnetism in twisted bilayer graphene,” [arXiv:1905.07651 \[cond-mat\]](https://arxiv.org/abs/1905.07651) (2019), arXiv: 1905.07651.
- [52] M. Aidelsburger, M. Lohse, C. Schweizer, M. Atala, J. T. Barreiro, S. Nascimbène, N. R. Cooper, I. Bloch, and N. Goldman, “Measuring the Chern number of Hofstadter bands with ultracold bosonic atoms,” *Nature Physics* **11**, 162–166 (2015).
- [53] Adolfo G. Grushin, Álvaro Gómez-León, and Titus Neupert, “Floquet Fractional Chern Insulators,” *Phys. Rev. Lett.* **112**, 156801 (2014).
- [54] F. D. M. Haldane, “Model for a Quantum Hall Effect without Landau Levels: Condensed-Matter Realization of the “Parity Anomaly”,” *Phys. Rev. Lett.* **61**, 2015–2018 (1988).
- [55] L. A. Ponomarenko, R. V. Gorbachev, G. L. Yu, D. C. Elias, R. Jalil, A. A. Patel, A. Mishchenko, A. S. Mayorov, C. R. Woods, J. R. Wallbank, M. Mucha-Kruczynski, B. A. Piot, M. Potemski, I. V. Grigorieva, K. S. Novoselov, F. Guinea, V. I. Fal’ko, and A. K. Geim, “Cloning of Dirac fermions in graphene superlattices,” *Nature* **497**, 594–597 (2013).
- [56] G. Trambly de Laissardière, D. Mayou, and L. Magaud, “Localization of Dirac Electrons in Rotated Graphene Bilayers,” *Nano Lett.* **10**, 804–808 (2010).
- [57] G. Trambly de Laissardière, D. Mayou, and L. Magaud, “Numerical studies of confined states in rotated bilayers of graphene,” *Phys. Rev. B* **86**, 125413 (2012).
- [58] One could equivalently start from *A-B* stacking, and we have checked that all of the results presented in this work hold equally for both choices.
- [59] Yuanbo Zhang, Tsung-Ta Tang, Caglar Girit, Zhao Hao, Michael C. Martin, Alex Zettl, Michael F. Crommie, Y. Ron Shen, and Feng Wang, “Direct observation of a widely tunable bandgap in bilayer graphene,” *Nature* **459**, 820–823 (2009).
- [60] Thiti Taychatanapat and Pablo Jarillo-Herrero, “Electronic Transport in Dual-Gated Bilayer Graphene at Large Displacement Fields,” *Phys. Rev. Lett.* **105**, 166601 (2010).
- [61] Hoi Chun Po, Liujun Zou, Ashvin Vishwanath, and T. Senthil, “Origin of Mott Insulating Behavior and Superconductivity in Twisted Bilayer Graphene,” *Phys.*

- Rev. X* **8**, 031089 (2018).
- [62] Liujun Zou, Hoi Chun Po, Ashvin Vishwanath, and T. Senthil, “Band structure of twisted bilayer graphene: Emergent symmetries, commensurate approximants, and Wannier obstructions,” *Phys. Rev. B* **98**, 085435 (2018).
- [63] R. de Gail, M. O. Goerbig, F. Guinea, G. Montambaux, and A. H. Castro Neto, “Topologically protected zero modes in twisted bilayer graphene,” *Phys. Rev. B* **84**, 045436 (2011).
- [64] Mikito Koshino, Noah F. Q. Yuan, Takashi Koretsune, Masayuki Ochi, Kazuhiko Kuroki, and Liang Fu, “Maximally Localized Wannier Orbitals and the Extended Hubbard Model for Twisted Bilayer Graphene,” *Phys. Rev. X* **8**, 031087 (2018).
- [65] Jon H. Shirley, “Solution of the Schrödinger Equation with a Hamiltonian Periodic in Time,” *Phys. Rev.* **138**, B979–B987 (1965).
- [66] Hideo Sambe, “Steady States and Quasienergies of a Quantum-Mechanical System in an Oscillating Field,” *Phys. Rev. A* **7**, 2203–2213 (1973).
- [67] André Eckardt and Egidijus Anisimovas, “High-frequency approximation for periodically driven quantum systems from a Floquet-space perspective,” *New J. Phys.* **17**, 093039 (2015).
- [68] Michael Schüler, Umberto De Giovannini, Hannes Hübener, Angel Rubio, Michael A. Sentef, and Philipp Werner, “Local Berry curvature signatures in dichroic angle-resolved photoelectron spectroscopy,” [arXiv:1905.09404 \[cond-mat\]](https://arxiv.org/abs/1905.09404) (2019), arXiv: 1905.09404.
- [69] The decreasing size of the light-induced gap due to increasing band flatness (smaller twist angles) is confirmed in Fig. 9 of the Appendix, in which we show the gap dependency on the driving amplitude for two smaller angles.
- [70] Riku Tuovinen, Enrico Perfetto, Robert van Leeuwen, Gianluca Stefanucci, and Michael A. Sentef, “Distinguishing Majorana Zero Modes from Impurity States through Time-Resolved Transport,” [arXiv:1902.05821 \[cond-mat\]](https://arxiv.org/abs/1902.05821) (2019), arXiv: 1902.05821.
- [71] Xiao Wang, Enrico Ronca, and Michael A. Sentef, “Cavity Quantum-Electrodynamical Chern Insulator: Route Towards Light-Induced Quantized Anomalous Hall Effect in Graphene,” [arXiv:1903.00339 \[cond-mat\]](https://arxiv.org/abs/1903.00339) (2019), arXiv: 1903.00339.
- [72] Lede Xian, Dante M. Kennes, Nicolas Tancogne-Dejean, Massimo Altarelli, and Angel Rubio, “Multi-flat bands and strong correlations in Twisted Bilayer Boron Nitride,” [arXiv:1812.08097 \[cond-mat\]](https://arxiv.org/abs/1812.08097) (2018), arXiv: 1812.08097.
- [73] D. M. Kennes, L. Xian, M. Claassen, and A. Rubio, “A New Twist in the Realization of One-Dimensional Physics,” [arXiv:1905.04025 \[cond-mat\]](https://arxiv.org/abs/1905.04025) (2019), arXiv: 1905.04025.
- [74] Alexander Kerelsky, Leo McGilly, Dante M. Kennes, Lede Xian, Matthew Yankowitz, Shaowen Chen, K. Watanabe, T. Taniguchi, James Hone, Cory Dean, Angel Rubio, and Abhay N. Pasupathy, “Magic Angle Spectroscopy,” [arXiv:1812.08776 \[cond-mat\]](https://arxiv.org/abs/1812.08776) (2018), arXiv: 1812.08776.
- [75] János K. Asbóth, László Oroszlány, and András Pályi, *A Short Course on Topological Insulators: Band Structure and Edge States in One and Two Dimensions*, Lecture Notes in Physics (Springer International Publishing, 2016).
- [76] Raffaele Resta and David Vanderbilt, “Theory of Polarization: A Modern Approach,” in *Physics of Ferroelectrics: A Modern Perspective*, Topics in Applied Physics (Springer Berlin Heidelberg, Berlin, Heidelberg, 2007) pp. 31–68.

Appendix A: Model

The tight-binding Hamiltonian is of the general form

$$H = \sum_i \epsilon_i c_i^\dagger c_i + \sum_{i \neq j} t_{ij} c_i^\dagger c_j, \quad (\text{A1})$$

where c_i^\dagger (c_i) creates (annihilates) an electron in the p_z orbital at the atomic position \mathbf{r}_i . We use hopping matrix elements as introduced in [57],

$$t_{ij} = n^2 V_{pp\sigma}(r_{ij}) + (1 - n^2) V_{pp\pi}(r_{ij}), \quad (\text{A2})$$

where $r_{ij} = \|\mathbf{r}_{ij}\|$ and $n = z_{ij}/r_{ij}$. For intralayer hopping, only the $V_{pp\pi}$ term contributes, as $z_{ij} = 0$. For interlayer hopping, both the $V_{pp\pi}$ and the $V_{pp\sigma}$ terms are nonzero ($z_{ij} = a_1$). A detailed illustration is shown in Fig. 6. Both hopping contributions are assumed to decay exponentially as a function of distance,

$$\begin{aligned} V_{pp\pi} &= \gamma_0 \exp[q_\pi(1 - r_{ij}/a)], \\ V_{pp\sigma} &= \gamma_1 \exp[q_\sigma(1 - r_{ij}/a_1)]. \end{aligned} \quad (\text{A3})$$

Here, $a = 1.418 \text{ \AA}$ is the intralayer nearest-neighbor distance, and $a_1 = 3.364 \text{ \AA}$ is the interlayer distance. The monolayer lattice constant of the triangular Bravais lattice is $a_0 = 2.445 \text{ \AA}$. For the nearest-neighbor hopping, $\gamma_0 = -3.24 \text{ eV}$, we add 20% to the DFT-fitted value in order to compensate for many-body effects beyond the employed DFT functional and in order to fit the van-Hove singularity in the tunneling density of states reported in 74. For the σ -related hopping we find $\gamma_1 = 0.55 \text{ eV}$. For the exponential decay we find fitting parameters, $q_\pi = 3.15$ and $q_\sigma = q_\pi \frac{a_1}{a}$. For the fictitious local potentials on the A and B sublattices that break inversion symmetry, ϵ_i , we assume different symmetry configurations, as shown in Fig. 7. We assume periodic Born-von Karman boundary conditions within in the x - y -plane. The Hamiltonian in momentum space is then calculated by a Fourier transforms, $c^\dagger(\mathbf{k}) = \sqrt{V_{\text{BZ}}^{-1}} \sum_i c_i^\dagger \exp(i\mathbf{k}\mathbf{r}_i)$ and $c(\mathbf{k}) = \sqrt{V_{\text{BZ}}^{-1}} \sum_i c_i \exp(-i\mathbf{k}\mathbf{r}_i)$, where V_{BZ} is the volume of the two-dimensional Brillouin zone.

Appendix B: Floquet dynamics

A circularly polarized laser driving field is included by coupling to a time-dependent external gauge field, $\mathbf{A}(t) = A_{\text{max}}(\mathbf{e}_x \sin(\Omega t) + \mathbf{e}_y \cos(\Omega t))$, where \mathbf{e}_x and \mathbf{e}_y denote the unit vectors in the spatial in-plane directions, via Peierls substitution of the form

$$t_{ij} \rightarrow \tilde{t}_{ij}(t) = t_{ij} e^{i\mathbf{A}(t)\mathbf{r}_{ij}}. \quad (\text{B1})$$

The main effect of the circularly polarized field is the breaking of time-reversal symmetry which induces a mass term to the Dirac fermions, as has been investigated for single-layer graphene [34, 40]. The peak electric

field strength is calculated from the amplitude of the vector potential by the relation, $E_{\text{max}} = \frac{A_{\text{max}}}{a_0} \Omega$, where $a_0 = 2.445 \text{ \AA}$, is the monolayer lattice constant. The resulting non-equilibrium state of the light-matter coupled system is periodic in time and can thus be analyzed by Floquet theory [65–67], which, by a Floquet-Bloch decomposition, maps the bare time-dependent Hamiltonian, $H(t+T) = H(t)$, to the time-independent Floquet Hamiltonian,

$$\mathcal{H}^{nm} = \frac{1}{T} \int_T dt e^{i(m-n)\Omega t} H(t) + \delta_{mn} m \Omega \mathbb{1}. \quad (\text{B2})$$

The integers m and n arise from the Floquet expansion of the time-dependent solutions of the Schroedinger equation,

$$|\Psi(t)\rangle = \sum_{m=-\infty}^{+\infty} \exp[-i(\epsilon + m\Omega)t] |u_m\rangle, \quad (\text{B3})$$

where ϵ is the Floquet quasi-energy and $|u_m\rangle$ the corresponding Floquet eigenfunction of the Floquet Hamiltonian. For the results shown in the main text we truncate the expansion after order $|m| = 2$ and use 200 sampling points to perform the integral over one period $T = 2\pi/\Omega$ in Eq. B2 numerically with the trapezoidal rule. We ensure convergence in the Floquet cutoff by means of the energy gap at the Dirac points with error smaller than 10^{-5} eV . In order to highlight the bands which overlap with the bare bands of the undriven system, in contrast to Floquet sidebands, we calculate the squared overlap, $\sum_\alpha |\langle \alpha | e_j \rangle|^2$, of the Floquet energy eigenstates, $|e_j\rangle$, with the energy eigenstates of the bare Hamiltonian, $H|\alpha\rangle = E_\alpha|\alpha\rangle$. Throughout this work we use units where $e = \hbar = c = 1$.

Appendix C: Berry curvature

The Berry curvature at a fixed momentum point can be defined by the Berry flux of an infinitesimally small loop around that point, divided by the enclosed area [75],

$$B^{(n)} = \lim_{\Delta k_x, \Delta k_y \rightarrow 0} \frac{F^{(n)}}{\Delta k_x \Delta k_y}, \quad (\text{C1})$$

where n refers to the corresponding band. On a discretized grid, the flux can be written in the form [76]

$$F^{(n)} \approx \text{Im} \left(\ln \prod_j \langle u_{n, \mathbf{k}_j} | u_{n, \mathbf{k}_{j+1}} \rangle \right). \quad (\text{C2})$$

Here, u_{n, \mathbf{k}_i} refers to the n -th energy eigenstate of the bare Hamiltonian and the Floquet Hamiltonian, respectively, at quasi-momentum \mathbf{k}_i , where $i \in \{1, 2, 3, 4\}$, as depicted in Fig. 8. We use a grid spacing of $\Delta k = 10^{-5} \text{ \AA}^{-1}$ for which the Berry curvature is sufficiently converged.

Appendix D: Light-induced energy gaps

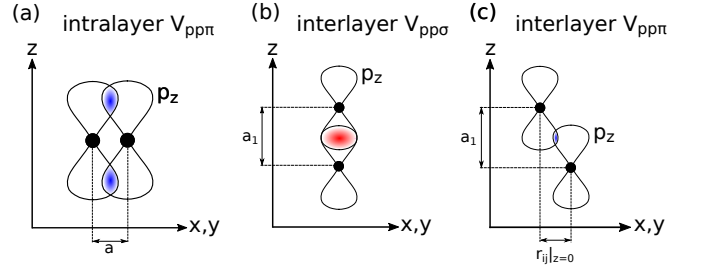


FIG. 6. Tight-binding hopping elements. Only p_z -orbitals are taken into account. (a) Intralayer hopping is restricted to $pp\pi$ terms. There are two channels for interlayer hopping: Vertical hopping is dominated by the $pp\sigma$ term (b). For non-vertical transitions also $pp\pi$ terms (c) contribute.

In Fig. 9 we show the light-induced energy gaps at the Dirac point without inversion-symmetry breaking fields for different twist angles as indicated. In all three cases, we choose as the photon frequency the Γ -point low-energy bandwidth, $\Delta_\Gamma = 2.23$ eV, which we extract from the equilibrium band structure for $\Theta = 7.34^\circ$. Importantly we find almost perfect scaling behavior with the bare Fermi velocity of single-layer graphene, as opposed to the actual Fermi velocity of the bilayer, for the largest twist angles of 7.34° . For smaller twist angles we find a deviation and the actual gap lies in between the one expected for single-layer graphene and the one for the bilayer.

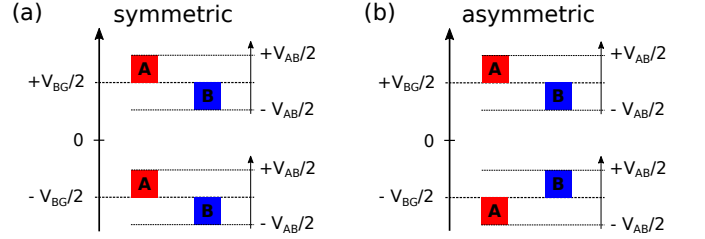


FIG. 7. Onsite potentials that break inversion symmetry. The backgate voltage, V_{BG} , is always chosen symmetric between both layers. (a) Symmetric \pm/\pm sublattice potential, V_{AB}^{sym} . (b) Asymmetric \pm/\mp sublattice potential, V_{AB}^{asym} .

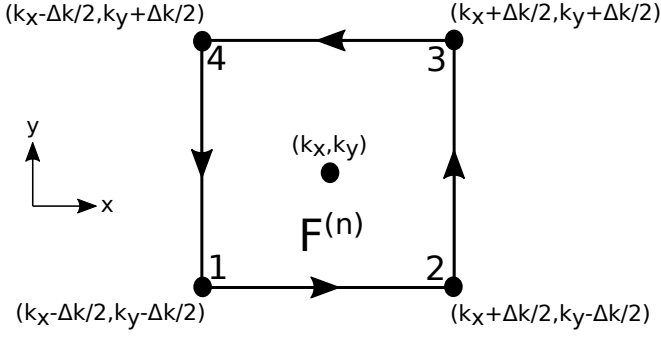


FIG. 8. Calculation of the Berry flux. The Berry flux of the n -th band, $F^{(n)}$, for a quasimomentum $\mathbf{k} = (k_x, k_y)$ is calculated by a closed loop along the eigenstates at position 1 to 4 in momentum space. Throughout we use a grid spacing of $\Delta k = 10^{-5} \text{ \AA}^{-1}$.

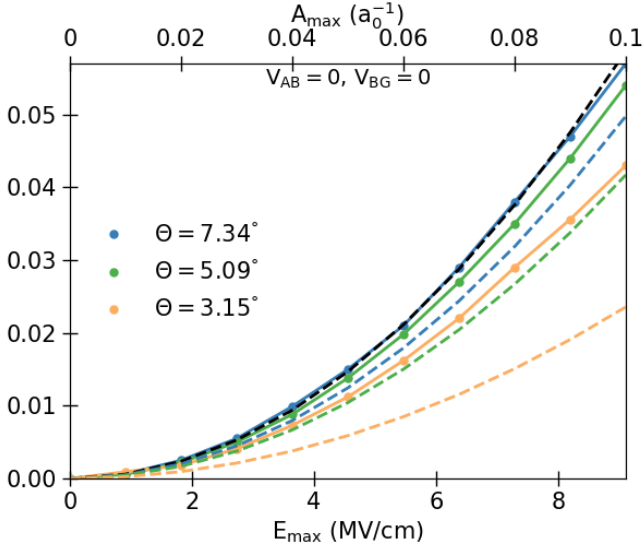


FIG. 9. Full energy gap at the Dirac point as a function of the driving amplitude for different twist angles, Θ (colored dots). In all three cases, the Floquet driving frequency is $\Omega = 2.23 \text{ eV}$. The black dashed line indicates the monolayer dependence of the gap on the driving amplitude and the Fermi velocity, $2(v_F^0 A_{\max})^2/\Omega$. The colored dashed lines indicate the corresponding relation for the twisted case.